A Composite L-Band HH Radar Backscattering Model for Coniferous Forest Stands

Guoqing Sun and *David S. Simonett*
Department of Geography, University of California, Santa Barbara, CA 93106

ABSTRACT: The radar backscattering model developed by Richards *et al.* (1987), has been improved and further tested in this research. The trunk term may now be calculated from the exact solution to the electromagnetic wave equations instead of the corner reflector equation. Rough surface models have been introduced into the radar model, so that the forward reflectance and the backscattering from the ground surface are now calculated from the same model and, thus, are consistent. The number of trees in an individual pixel is assumed to be Poisson distributed, with tree height in a stand log-normally distributed. The simulated results show that the match of backscattering coefficients for eight forest stands between SIR-B image data and the simulated results are satisfying, and that the trunk term now seems to be convincingly established as the dominant term in the L-band HH radar return from coniferous forest stands.

INTRODUCTION

IN A EARLIER PAPER (Richards *et al.*, 1987), we introduced an L band HH radar backscatter model of a coniferous forest stand, in which four scattering components were considered: volume scatter from foliage, direct backscatter from the ground surface, bistatic scatter from trunk to ground and then reflection back to the radar, and scatter from foliage to ground and then reflection back again. This model has been improved through the following implementations:

- Bistatic scatter from a dielectric cylinder is calculated using the exact solution of wave propagation equations instead of a corner reflector model;
- Rough surface models have been introduced to the model so that backscatter and forward reflectance of the underlying surface can be calculated simultaneously and therefore consistently; and
- The Poisson distribution of trees within a stand and the Lognormal distribution of the tree height are assumed based on earlier research results (Li and Strahler, 1985).

The numbers of pixels simulated are the same as that used from SIR-B. The input parameters to the model include average tree numbers per pixel, the average tree height, variance of tree height, and wavelength, with assumptions on extinction coefficient (κ), volume scattering coefficient (η) for foliage, relative dielectric constants for tree trunk and soil, and roughness parameters of the soil surface.

The following sections will describe the test sites, SIR-B image data, field sampling data, and the modeling process.

STUDY SITES AND DATA AVAILABLE

The study area is located south-east of Mount Shasta, in Northern California. Most of the forest stands are natural stands of Ponderosa Pine, with underlying surfaces which are very level. Tree height in the area ranges from about 10 to 50 metres, and densities vary from 15 to 50 trees per $[25m]^2$ radar resolution cell.

SIR-B images with three incidence angles (29.7°, 53.8°, 63.8°) were obtained during the period 8 to 11 October 1984. One of them (53.8°) missed about one half of the study area.

The lowest digital number (DN) in a SIR-B scene, which is in the shadow of Mount Shasta, is assumed as the noise floor and has been subtracted from the image. The DN of the images were converted to relative backscattering coefficients by the following equation:

$$\sigma^0 = 10 * \log((\mathrm{DN}^2 - \mathrm{DN}_0^2)/S^2) - \sigma_a$$

where DN_0 is noise level, σ_a is a constant for matching SIR-B data with the simulated results at one point, and S is the scale factor of the images to convert the recorded signal from radar receiver to image DN during the image processing.

Figure 1 shows the TM image of Band 3 and SIR-B image at an incidence angle of 29.7° of the test sites. The eight different forest stands are outlined in the TM image.

Extensive field sampling was carried out a year after the SIR-B flight, with sampling of forest stands of various densities. The measurements include tree species, tree count, DBH (diameter at breast height), total height, height to widest part of crown, width of crown, and the positions for each sampled tree, which allows for the analysis of tree distribution pattern in a stand. Four to six plots, aggregating to about 150 trees for each stand, were sampled.

The relationships between the tree total height, and height to the widest part of crown with respect to DBH, were established by regression analysis and serve as inputs to our model.

FOUR COMPONENTS OF THE FOREST STAND MODEL

Four backscattering mechanisms have been used as depicted in Figure 2: These are foliage volume scattering, surface scattering from an underlying soil layer, bistatic scattering from the foliage to the ground and back to the radar, and bistatic scattering from the trunk onto the ground and again followed by reflection from ground to the radar. The last two mechanisms can also take place in the opposite directions.

The first component, foliage volume scattering, is given by the water cloud model (Attema and Ulaby, 1978)

$$\sigma_v^0 = \frac{\eta \cos\theta}{2\kappa}[1 - \exp(-2\kappa h_c \sec\theta)]$$

in which θ is the local incidence angle and h_c is the effective depth of the canopy, and η is a volume scattering coefficient and κ is the canopy extinction coefficient, values for both of which are often found experimently.

The direct backscattering from the soil surface is *the second component* in the model. Depending on the conditions of the ground surface, the small perturbation model and Kirchhoff model have been used to calculate the backscattering and specular reflection of the surface. Most surfaces in our study area meet the requirements of the small perturbation model. The backscattering is given by (Dobson and Ulaby, 1986)

$$\sigma_s^0 = \frac{A_s}{A} \times 4(k\sigma)^2(kL)^2\cos^4\theta \exp[-(kL\sin\theta)^2] \mid R_{hh} \mid^2 \exp(-2\kappa h_c \sec\theta)$$

and the forward reflectance of the surface is

PHOTOGRAMMETRIC ENGINEERING AND REMOTE SENSING,
Vol. 54, No. 8, August 1988, pp. 1195–1201.

0099-1112/88/5408–1195$02.25/0

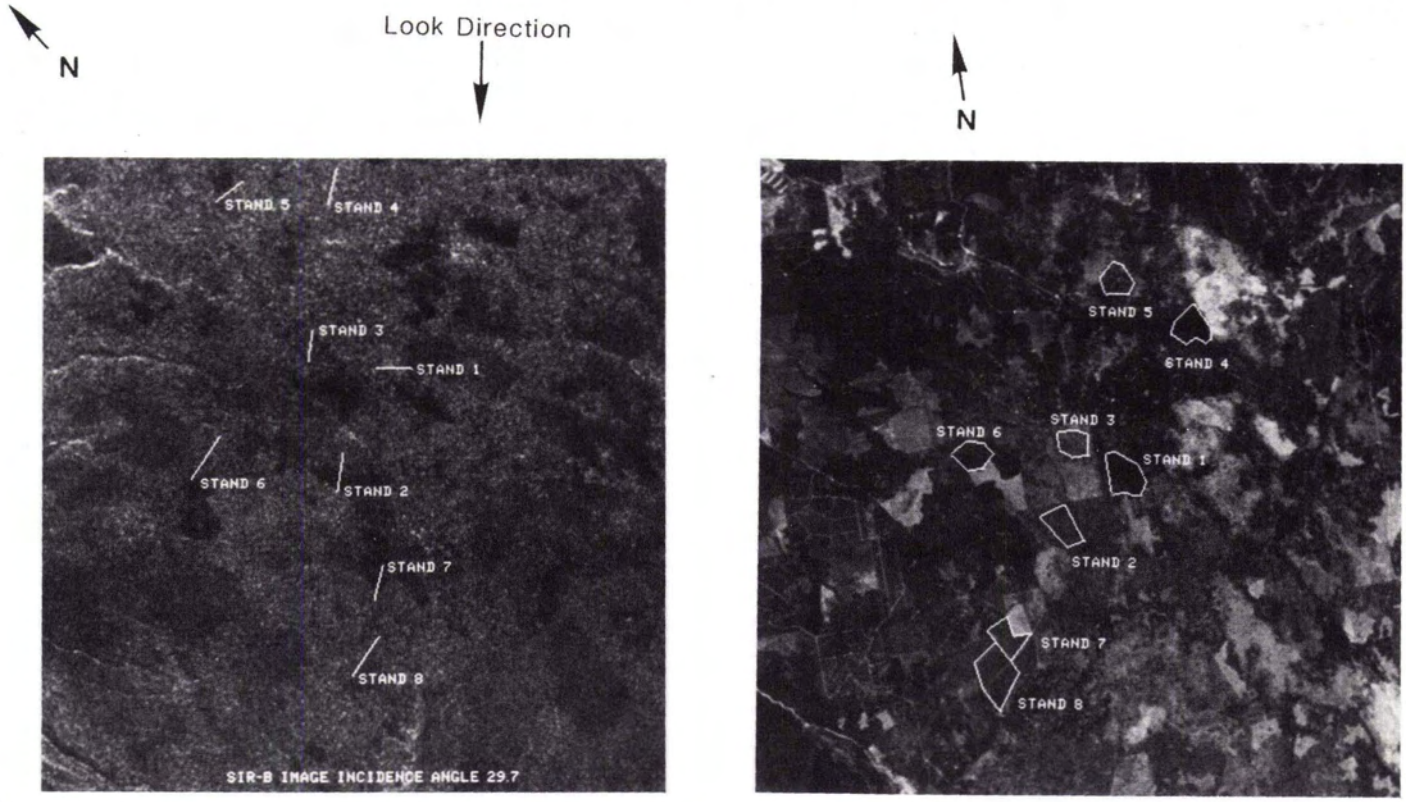

FIG. 1. SIR-B image at an incidence angle of 29.7° and TM band 3 image of study area, located southeast of Mount Shasta. Stands 1 through 6 are natural forest stands and stands 7 and 8 are plantations of Ponderosa pine.

$$\rho_s = R_{hh} \exp\left[-2(k\,\sigma\cos\theta)^2\right]$$

where A_s is the surface area not obscured by trunks and A is the area of a pixel. R_{hh} is Fresnel reflectance of the surface. σ and L are the RMS roughness and surface correlation length, respectively.

The third component due to the interaction between canopy and ground derived from the model by Engheta and Elachi (1982) can be written as

$$\sigma^0_{v-s} = h_c\eta \mid \rho_s \mid^2 \exp(-2\alpha)[2 + \mid \rho_s \mid^2 \exp(-\alpha)\sin h(\alpha)/\alpha]$$

The fourth component is the bistatic scattering from the tree

where $\alpha = \kappa h_c \sec\theta$.

The fourth component is the bistatic scattering from the tree trunk onto the ground and back to the sensor. We assume that the tree trunks are smooth in the surface and can be modeled as dielectric cylinders, and that trees are randomly distributed in a homogeneous forest stand.

For a dielectric cylinder with length h_t and radius b, which satisfies $h_t >> 2b$, the bistatic scattering cross section in the far zone is (Ruck *et al.*, 1970, pp 302–307)

$$\sigma^t(\theta,\theta_s,\phi') = \frac{kh_t^2}{\pi}\sin^2\theta_s\sigma^c(\theta,\phi')\left[\frac{\sin(k(\cos\theta+\cos\theta_s)h_t/2)}{k(\cos\theta+\cos\theta_s)h_t/2}\right]^2$$

where $\sigma^c(\theta,\phi')$ is scattering width of a dielectric cylinder with infinite length.

In the case of the HH mode, the scattering width in the specular direction ($\phi' = 0$) is

$$\sigma^c(\theta,0) = \frac{4}{k\sin^2\theta}\mid \sum_{n=-\infty}^{n=\infty}(-1)^n C_n \mid^2.$$

If the cylinder material has a relative permeability, $\mu_2 = 1$, and dielectric constant, ϵ_2, then the exact series solution coefficients are (Ruck *et al.*, 1970, pp. 273)

$$C_n = -\frac{M_n N_n - q_n^2 J_n(x_0) H_n^{(1)}(x_0) J_n^2(x_1)}{P_n N_n - [q_n H_n^{(1)}(x_0) J_n(x_1)]^2}$$

where J and H and Bessel functions of first kind and Hankel functions, respectively, and

$$x_0 = kb\sin\theta,$$

$$x_1 = kb\sqrt{\epsilon_2 - \cos^2\theta},$$

$$q_n = \frac{n\cos\theta}{kb}\left[\frac{1}{\epsilon_2-\cos^2\theta} - \frac{1}{\sin^2\theta}\right],$$

$$P_n = r_1 H_n^{(1)}(x_0)\,J_n'(x_1) - s_0 H_n^{(1)\prime}(x_0) J_n(x_1),$$

$$N_n = s_1 H_n^{(1)}(x_0) J_n'(x_1) - s_0 H_n^{(1)\prime}(x_0) J_n(x_1),$$

$$M_n = r_1 J_n(x_0) J_n'(x_1) - s_0 J_n'(x_0) J_n(x_1),$$

and

$$s_0 = \frac{1}{\sin\theta},\ s_1 = \frac{\epsilon_2}{\sqrt{\epsilon_2-\cos^2\theta}},\ r_1 = \frac{1}{\sqrt{\epsilon_2-\cos^2\theta}}$$

On the assumption that the cylinder has a smooth surface, there will be no direct backscattering from the trunk at oblique incidence. The contribution of the tree trunk to backscattering is assumed to be a part of the bistatic scattering from the tree trunk reflected toward the radar by the soil surface. For scattering in the specular direction, $\theta_s = 180° - \theta$ and $\phi' = 0$, the scattering cross section from the finite cylinder is

$$\sigma^t(\theta) = \frac{kh_t^2}{\pi}\sin^2\theta\sigma^c(\theta,0)$$

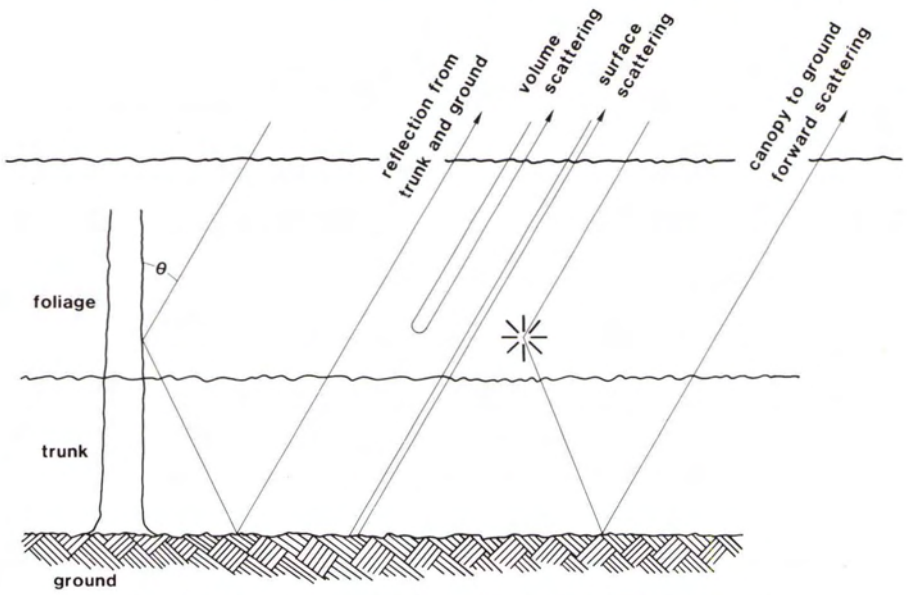

FIG. 2. Backscatter components employed in the forest stand model.

If there are n trees in a pixel, and coherent summation is used, the total radar cross section of tree trunks will be

$$\sigma_t = | \sum_{i=1}^{i=n} \sqrt{\sigma_i^t}\, e^{j\phi_t} |^2$$

where σ_i^t, ϕ_i are the radar cross section and the phase angle of radar return from the i_{th} tree.

For denser forest stands, where the tree number in a pixel is large, incoherent summation may be assumed: i.e.,

$$\sigma_t = \sum_{i=1}^{i=n} \sigma_i^t.$$

Then the backscattering coefficient of the fourth component can be written as

$$\sigma_{t-g}^0 = \frac{2}{A} | \rho_s |^2 \sigma_t e^{-2\kappa h_c/\cos\theta}.$$

In the above formulation, note that the radar cross section is divided by the area of a pixel and multiplied by the two-way transmission coefficient and a factor 2, taking into account the mirror effect of the ground surface.

The incident rays penetrate the first layer, and are scattered and attenuated in this layer. The rays illuminating the soil surface are backscattered toward the radar after being attenuated by the first layer again. The rays illuminating the tree trunks undergo a more complex process. The incident rays will be reflected in the specular direction and then reflected again by the soil surface toward the radar. The total backscattering coefficient of a pixel will be

$$\sigma^0 = \sigma_v^0 + \sigma_{t-g}^0 + \sigma_s^0 + \sigma_{v-s}^0$$

IMPLEMENTATION OF MODELING

Our radar backscatter model is used to generate the statistics of radar backscatter for pixels constituting a forest stand of given characteristics. Thus, the stand-specific data needs to be defined first.

The relation between tree height and DBH (diameter at breast height) has been determined from field measurements (Figure 3). A linear regression relation DBH $= 0.00531 + 0.0172 \times h$ with

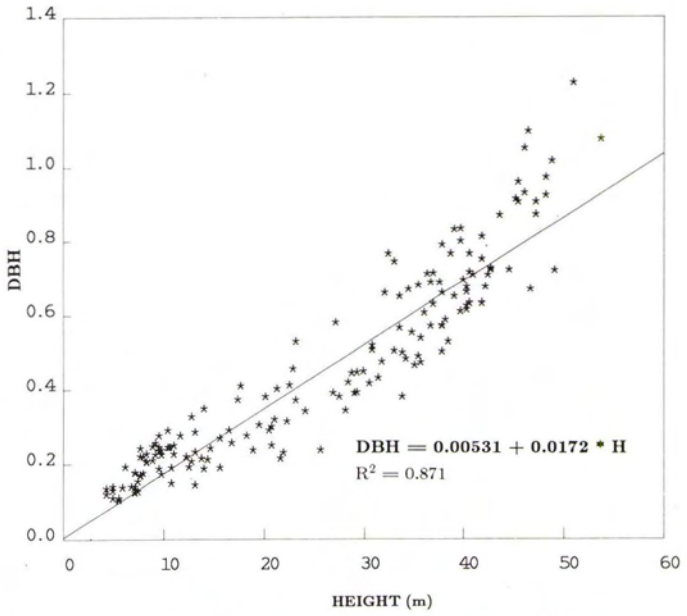

FIG. 3. Linear regression of DBH versus height for Ponderosa pine.

$R^2 = 0.87$ was used here based on previous research (Li, 1981), even though another regression DBH $= 0.155 + 0.000339 \times h^2$ has higher $R^2 = 0.90$. The equivalent trunk (cylinder) height (h_t) has been chosen to be the length of the trunk between the ground and the bottom of the crown plus two thirds of the actual crown height. The effective canopy depth (h_c) was determined by measuring from the top of the tree down to the height above the ground at which the crown was widest. Because of randomness of tree numbers and heights in an individual pixel, the equivalent planar thickness of the canopy is calculated from the average tree height in the pixel, and assumed to be equal to the average measured canopy height of the trees, based on the assumption that the forest canopy is nearly closed. Another option for estimating canopy thickness is to establish an equivalent slab of canopy with the same volume as the trees in a

pixel, having regard to the individual tree canopies comprising simple shapes such as cones.

The distribution of tree density within a stand is assumed to be Poisson distributed based on the previous work by Strahler and Li (1981, 1985). The basic assumption in applying a Poisson distribution is that trees occur randomly, i.e., all locations are equilikely and independent. This is a reasonable assumption for undisturbed natural forest stands, and may also be suitable for older plantations which have experienced many thinnings. The field work by Strahler and Li (1981) in the specific target stands, which belong to the same natural forest and mainly consist of Ponderosa pine as did our study area, has shown a reasonable fit to the Poisson model for intermediate and dense stands at pixel (quadrat) sizes of 10 to 30 m.

Previous work by Johnson (1949), Hafley Scheuner (1977), and Li and Strahler (1985) has indicated that the heights (diameters) of trees of a given species vary in a log-normal fashion in reasonably closed stands. Figure 4 shows a Quantile-Quantile plot of log(DBH) versus normal distribution. The bulk of the data is distributing along the straight line, which indicates that this is basically a log-normal distribution, but with shorter tails in both low and high ends indicated by departures of the data from log-normality. In the low end this is because only trees with DBH greater than three inches were measured. On the other hand, trees can never grow infinitely as the theoretical distribution, which causes the shorter tail in the high end. Accordingly, in the simulation we have set limits for both ends. When the tree height generated from the simulation is greater than the high limit or less than the low limit, the tree is assigned to the average height, as an input parameter.

In order to reduce the computation of radar cross sections of several tens of cylinders in each pixel, a look-up table has been calculated for each radar incidence angle. Figure 5 shows the curve stored in a look-up table for incidence angles of 29.7°, which includes the radar cross section of cylinders of height from 2.0 to 80 metres in increments of 0.1 meter. The radius of the cylinder is determined from the regression relation derived from field measurements. The curves for incidence angles of 53.8° and 63.8° have basically the same shape as that shown in the Figure 5 except that there are slightly different ripples when trees are smaller.

Different methods for summing the radar cross section from

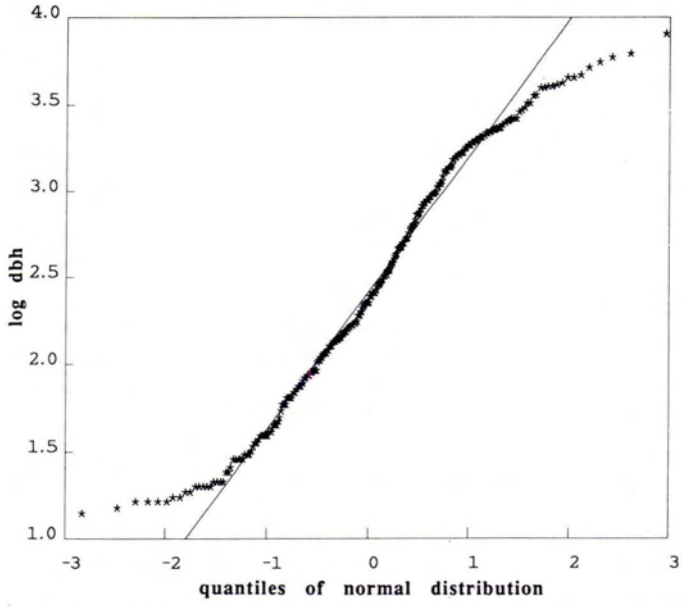

FIG. 4. Quantile-Quantile plot of log (DBH) versus normal distribution.

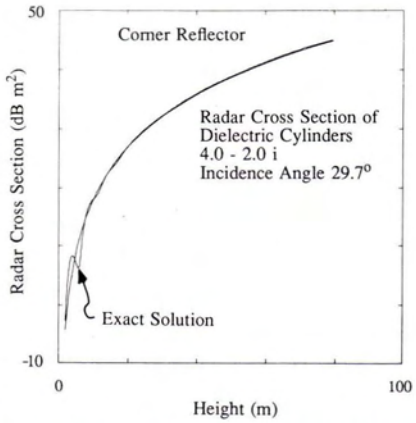

FIG. 5. Radar cross sections of dielectric cylinders over a plane with reflectance 1.0 at an incidence angle of 29.7°. Diameter and height are related according to the regression in Figure 3. Also shown is the radar cross section calculated from the corner reflector model at the same incidence angle.

all tree trunks in a pixel have been tested. The results given in this paper are all derived from coherent summation, in which each trunk has been assigned a random phase with $0 - 2\pi$. Also the four adjacent simulated pixels have been averaged to imitate 4-look radar images.

Assuming an average tree number n_m in a rectangular pixel of the radar image, and that average tree height and variance in a forest stand are known, simulation of a pixel in the radar image is as follows:

- generate the number of trees in the pixel from the Poisson distribution and generate a height for each of the trees in the pixel from a lognormal distribution;
- divide the pixel area into a 0.5-m grid and position these trees in the pixel by generating (x, y) coordinates for each tree from uniform distributions; i.e., randomized spatially, with equal probability of drawing any grid position, but excluding previously occupied grid positions;
- calculate the radius of each tree from its height and determine the equivalent depth of canopy from the averaged tree height in the pixel using the relations derived from field data; and
- calculate the backscattering coefficients for each component and then sum them.

The same number of pixels as in the SIR-B images have been simulated for a forest stand and the mean and standard deviation of the backscattering coefficient have been compared with the SIR-B images.

SIMULATION RESULTS

Figure 6 shows the simulated curves of backscattering coefficient versus incidence angle. Also shown in figure are the four model components. In order to show the angular behavior of the model more clearly for illustrative purposes, average tree number and tree height in the forest stand were fixed and chosen as 20 trees and 20 metres, respectively, for this figure, though in the actual comparisons for each pixel, tree number and height employed the Poisson and log-normal distributions. Other parameters used in the simulation are as follows: wavelength 0.235m; dielectric constants of tree trunk 4.0–2.0i; of soil 7.0–1.5i; volume backscattering and extinction coefficients of canopy $0.02\text{m}^2\text{m}^{-3}$ and $0.1\ \text{Npm}^{-1}$. The soil surface is assumed to meet the requirements of the small perturbation model and 0.02 m and 0.14 m were used for σ and L.

The curves clearly show that, when the incidence angles are

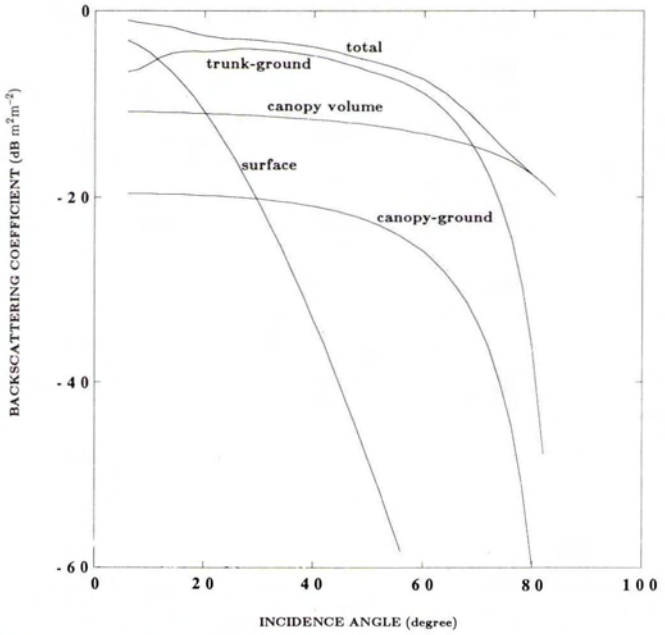

FIG. 6. Simulated backscattering coefficient as a function of incidence angle, for 20 trees 20 metres high. Shown also are the individual backscattering components.

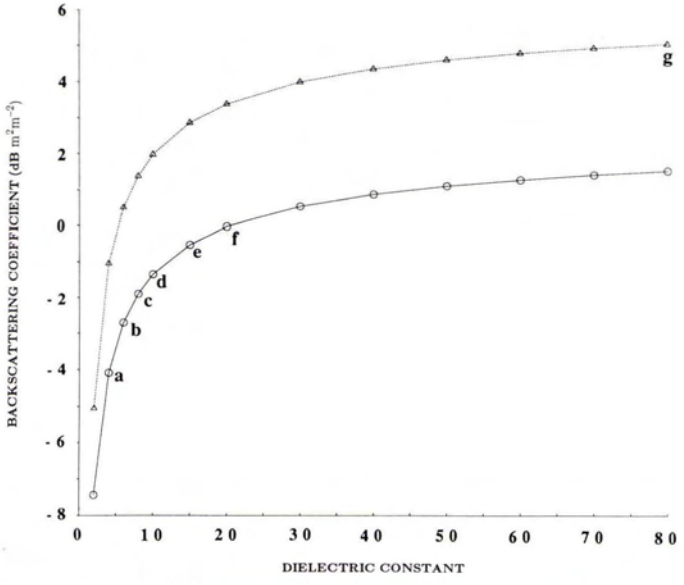

FIG. 7. Simulated backscattering coefficient from forest stand 1 under various surface conditions at an incidence angle of 29.7°. The curve with the △s is for a smooth surface, and that with the ○s for a slightly rough surface, which is assumed to satisfy the requirements of the small perturbation model.

small ($\theta = 10°$), the surface term is important, while the volume scattering term becomes dominant when the incidence angle is large ($\theta > 65°$–$70°$), whereas for intermediate values of $\theta = 10°$–$65°$, the trunk term is dominant. The model seems to have good angular behavior, consistent with both theoretical and empirical expectations even though there is no appropriate SIR-B data to test it.

The sensitivity of backscattering to change in surface properties is shown in Figure 7, in which we plot simulated backscattering coefficients from a forest stand under various surface conditions ranging from dry soil to standing water. Points "a" through "f" represent a range of actual surfaces with various moisture contents, and point "g" the surface with standing water under trees. A 3 to 6 dB increase in backscattering coefficient from forest stands when there was standing water under it, observed by some investigators (Engheta and Elachi, 1982; Ormsby *et al.*, 1985; Stone and Woodwell, 1985; Hoffer *et al.*, 1985; Imhoff *et al.*, 1985; Paris and Parrish, 1985 a, 1985 b), is a direct result of the corresponding change of surface forward reflectance. As shown in Figure 7, the equivalent range for our model is 3 to 8 dB. Please note that this effect can only be explained when the interaction terms are dominant. Of the two interaction terms in our model, the trunk term is always much the larger.

Figure 8 shows comparisons between simulated backscattering coefficients and SIR-B data over eight Shasta forest stands at three incidence angles. Stands 1 through 6 are natural forest stands and 7 and 8 are plantations of about 20 years old. Be-

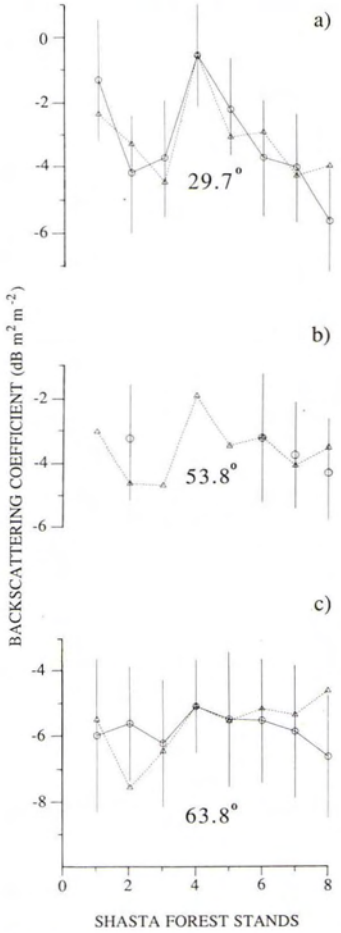

FIG. 8. Observed (○) and simulated (△) backscattering coefficients for eight different forest stands. Results are shown for six natural forest stands (1–6) and two plantations (7–8). The vertical bars around the means of SIR-B data show the range of one standard deviation. The SIR-B data have been adjusted to match the simulated data at one point (stand 4 in plots a and c, and stand 6 in plot b). Figure 8a is for 29.7°, 8b for 53.8°, and 8c for 63.8°.

cause there is no absolute calibration in the SIR-B images, the SIR-B data were adjusted by subtracting a variable (for different images) dB level to match the simulated results at one point (stand 4 in Figures 8a and 8c, and stand 6 in Figure 8b). The error bars around means in the plots show the range of one standard deviation of SIR-B data. At an incidence angle of 29.7° (Figure 8a) the remaining agreement between simulated and SIR-B data is satisfying. The simulated data fall well within one standard deviation of SIR-B data except stand 8. At 63.8° there are two major departures; stand 2 and 8. There are only four stands covered by the SIR-B image of 53.8°.

Generally, the mismatch may arise from the inappropriate sampling of both field and SIR-B images. It is quite often found that a single plot selected from random or systematic sampling procedures not quite suitable for representing the area, especially when the number of sampled plots is relatively small as in our study. A SIR-B subimage of 400 pixels for each forest stand was selected to represent a given forest stand. However, there is uncertainty in the estimated backscattering coefficients for each stand, the accumulation of which may change the agreement between simulated and SIR-B data. A rigorous statistical comparison based on certain confidence levels will subsequently be performed to ensure the realistic behavior of our model. The mismatch of stand 8, which is a young plantation, in both incidence angles may also be due to the existence of an understory of tangled Ceanothis shrubs in the stand, which is ignored in our model at present.

Figure 9 plots the one standard deviation error bars for simulated data, from which we can see that the variances of the data are quite similar to that of the SIR-B data. The spread of the simulated data results from both the randomness of tree number and height in a pixel and the coherent summation of radar cross sections of tree trunks. The similarity of variances between simulated and SIR-B data indicates that the fading phenomenon in SAR images is properly simulated in our model.

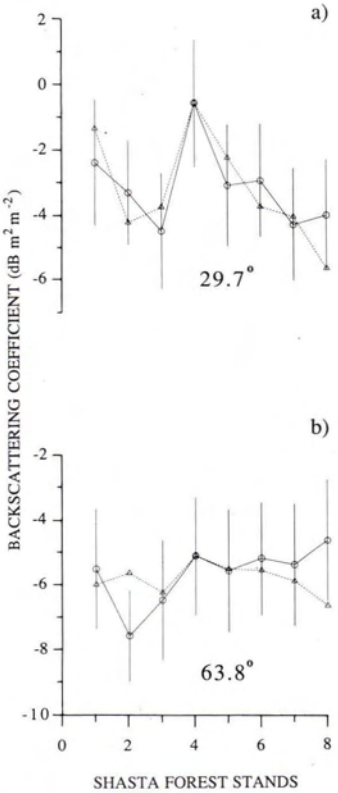

FIG. 9. Shown here are the ranges of plus and minus one standard deviation about the means from simulation. The variances of the simulated (○) are very similar to those of observed (△) data in Figure 8.

CONCLUDING REMARKS

In comparison to earlier studies which primarily were concerned with foliage contributions, the inclusion of the trunk term in our composite model proved to be critical to explain the radar returns from coniferous forest stands in terms of both mean and variance of backscattering. Without the trunk term, the trends of backscattering from different forest stands observed experimentally cannot be accounted for (Richards *et al.*, 1987). Tree trunks constitute the major part of living material in coniferous forest stands. Also, the scattering involved with the trunk term is forward scattering. Hence, the trunk term becomes dominant in the L Band HH radar return, where both backscattering and extinction of foliage is relatively small.

The volume backscattering coefficient η and extinction coefficient κ of the foliage layer used in this simulation are 0.02 and 0.1, respectively. In the case of the extinction coefficient, our estimate is derived through comparing the backscattering of SIR-B pixels with and without the Active Radar Calibrator, and is about 0.06 Npm^{-1} or $-0.25 dBm^{-1}$. The volume backscattering coefficient η was determined from κ according to Attema and Ulaby (1978). While this estimation may be questionable, the sensitivity of the model to substantial changes in η is low because the volume scattering term is not a dominant term in most cases at this (L-Band) long wavelength. The η and κ should not be the same for different forest stands. An appropriate model, by which the η and κ may be estimated from tree density, size, and shape, is now under development for introduction to our model.

The comparisons of radar cross section of dielectric cylinders calculated from the exact solution with that calculated using the corner reflector model showed that they are in close agreement at an incidence angle of 29.7° (Figure 5). It is also worth noting that the model behaves much better at an incidence angle of 29.7° than at 63.8°, which probably arises because (1) at higher incidence angles the volume term tends to become dominant (because this term is almost the same for many stands, it follows that discrimination between different forest stands is correspondingly reduced) and (2) the signal to noise ratio of the image for 63.8° is low. The most suitable SIR-B images to be used for inversion seem to lie at small incidence angles. If images close to 30° (29.7°) were to be used for inversion, the corner reflector model could be used to simplify the inversion procedure.

ACKNOWLEDGMENTS

This study was supported by a NASA contract through the Jet Propulsion Laboratory as part of the SIR-B Science Investigations (contract # JPL 956887).

REFERENCES

Attema, E. P. W., and F. T. Ulaby, 1978. Vegetation modeled as a water cloud, *Radio Science*, Vol. 13, No. 2, pp 357–364.

Dobson, M. C., and T. Ulaby, 1986. Preliminary evaluation of the SIR-B response to soil moisture, surface roughness, and crop cover, *IEEE Transactions on Geoscience and Remote Sensing*, Vol. GE-24, No. 4, pp. 517–526.

Engheta, N., and C. Elachi, 1982. Radar scattering from a diffuse vegetation layer over a smooth surface, *IEEE Transactions on Geoscience and Remote Sensing*, Vol. GE-20, No. 2, pp 212–216.

Hafley, W. I., and H. T. Scheuner, 1977. Statistical distributions for fitting diameter and height data in even aged stands, *Can. For. J. Res.*, Vol. 7, pp. 481–489.

Hoffer, R. M., and P. W. Mueller, 1985. Assessing forest resources using multiple incidence angle SIR-B data. *IEEE Cat. No. 85CH2162-6, Digest 1985 Int. Geosci. and Remote Sensing Symp.*, Vol. II, 572. Amherst, Massachusetts.

Imhoff, M. L., M. Story, and M. Snyder, 1985. Vegetation penetration- and forest Biomass assessment using multi-incidence angle space-borne radar. *IEEE Cat. No. 85CH2162-6, Digest 1985 Int. Geosci. and Remote Sensing Symp.*, Vol. II, 576. Amherst, Massachusetts.

Johnson, N. L., 1949. Bivariate distributions based on simple translation systems, *Biometrika*, Vol. 36, pp. 297–304.

Li, X. W., 1981. *An Invertible Coniferous Canopy Reflectance Model*, M. A. Thesis, University of California, Santa Barbara.

Li, X. W., and A. H. Strahler, 1985. Geometric-optical modeling of a coniferous forest canopy, *IEEE Transactions on Geoscience and Remote Sensing*, Vol. GE-23, pp. 705–721.

Ormsby, J. P., B. J. Blanchard, and A. J. Blanchard, 1985. Detection of lowland flooding using active microwave systems, *Photogrammetric Engineering and Remote Sensing*, Vol. 51, pp. 317–328.

Paris, J. F., and J. B. Parrish, 1985a. Use of shuttle imaging radar (SIR-B) for crop surveys in an irrigated agricultural region in California. *IEEE Cat. No. 85CH2162-6, Digest 1985 Int. Geosci. and Remote Sensing Symp.*, Vol. II, 578. Amherst, Massachusetts.

———, 1985b. Use of L-band, multipolarization synthetic aperture radar (SAR) image data for irrigated crop surveys. *IEEE Cat. No. 85CH2162-6, Digest 1985 Int. Geosci. and Remote Sensing Symp.*, Vol. II, 684. Amherst, Massachusetts.

Richards, J. A., Guo-Qing Sun, and D. S. Simonett, 1987. L-band radar backscatter modeling of forest stands, *IEEE Transactions on Geoscience and Remote Sensing*, Vol. GE-25, No. 4, pp. 487–498.

Ruck, G. T., D. E. Barrick, W. D. Stuart, and C. K. Krichbaum, 1970. *Radar Cross Section Handbook*, Plenum Press, New York. Vol. 1, pp. 273, 302–307.

Strahler, A. H., and X. W. Li, 1981. An invertible coniferous forest canopy reflectance model, *Fifteenth International Symposium on Remote Sensing of the Environment*, Ann Arbor, Michigan, May, pp. 1–8. *IEEE Transactions on Antennas and Propagation*, Vol. AP-28, No. 4, pp. 538–545.

(Received 4 October 1987; accepted 1 February 1988; revised 11 April 1987)

Forthcoming Articles

Robert C. Balling, Jr. and *Sandra W. Brazel*, High-Resolution Surface Temperature Patterns in a Complex Urban Terrain.
Jack Bryant, On Displaying Multispectral Imagery.
Pat S. Chavez, Jr. and *Jo Ann Bowell*, Comparison of the Spectral Information Content of Landsat Thematic Mapper and SPOT for Three Different Sites in the Phoenix, Arizona Region.
Emilio Chuvieco and *Russell G. Congalton*, Using Cluster Analysis to Improve the Selection of Training Statistics in Classifying Remotely Sensed Data.
S. A. Drury and *G. A. Hunt*, Remote Sensing of Laterized Archaean Greenstone Terrain: Marshall Pool Area, Northeastern Yilgarn Block, Western Australia.
Robert C. Dyer, Remote Sensing Identification of Tornado Tracks in Argentina, Brazil, and Paraguay.
J. H. Everitt, D. E. Escobar, A. H. Gerbermann, and *M. A. Alaniz*, Detecting Saline Soils with Video Imagery.
Clive S. Fraser and *Raymond L. Denham*, A Cine-Photogrammetric System for the Monitoring of a Dynamic Event Underwater.
Tung Fung and *Ellsworth LeDrew*, The Determination of Optimal Threshold Levels for Change Detection Using Various Accuracy Indices.
D. J. Gugan and *I. J. Dowman*, Topographic Mapping from SPOT Imagery.
Tuomas Häme and *Markku Rantasuo*, Shuttered Camera—Aerial Color Video Imaging in the Visible and Near Infrared.
Mohsen Mostafa Hassan, Filtering Digital Profile Observations.
Carolyn J. Merry, Harlan L. McKim, Nancy LaPotin, and *John R. Adams*, Use of SPOT HRV Data in the Corps of Engineers Dredging Program.
David B. Nash, Detection of a Buried Horizon with a High Thermal Diffusivity Using Thermal Remote Sensing.
David P. Paine and *Richard J. McCadden*, Simplified Forest Inventory Using Large-Scale 70-mm Photography and Tarif Tables.
Paul G. Pilon, Philip J. Howarth, Ronald A. Bullock, and *Peter O. Adeniyi*, An Enhanced Classification Approach to Change Detection in Semi-Arid Environments.
J. D. Pos, L. P. Adams, and *F. A. Kilner*, Synoptic Wave Height and Pattern Measurements in Laboratory Wave Basins Using Close-Range Photogrammetry.
Dan Rosenholm and *Kennert Torlegard*, Three-Dimensional Absolute Orientation of Stereo Models Using Digital Elevation Models.
John W. Salisbury and *N. M. Milton*, Thermal Infrared (2.5- to 13.5-μm) Directional Hemispherical Reflectance of Leaves.
Mark R. Shortis, Precision Evaluations of Digital Imagery for Close-Range Photogrammetric Applications.
Andrew K. Skidmore and *Brian J. Turner*, Forest Mapping Accuracies Are Improved Using a Supervised Nonparametric Classifier with SPOT Data.
Howard Turner, Photogrammetry and Real-Time Graphics in Engineering Applications.
E. Lynn Usery and *Roy Welch*, A Raster Approach to Topographic Map Revision.
Walter E. Westman and *Curtis V. Price*, Detecting Air Pollution Stress in Southern California Vegetation Using Landsat Thematic Mapper Band Data.